Renewable Energy and Smart Systems Journal Vol. 2, No. 1, 2026: 101-119

Renewable Energy and Smart Systems

journal homepage: https://sanad.iau.ir/journal/res

Improved Disturbance Rejection in Sensorless DFIG Wind Turbines Using Fuzzy Fractional-Order Control

Seyed Reza Mosayyebi[1]*, Mojtaba Ajoudani[1], Ramazan Teimouri Yansari[2]

[1] *Department of Electrical Engineering, BG.C., Islamic Azad University, Bandargaz, Iran.*
[2] *Department of Computer Engineering, BG.C., Islamic Azad University, Bandar Gaz, Iran.*

Article info

Keywords:
Doubly-fed Induction Generator (DFIG)
Sensorless Control
Fuzzy Logic
Fractional-order Control
Active Disturbance Rejection Control (ADRC)

Article history:
Received: 18 02 2026
Accepted: 22 02 2026

Abstract

This paper introduces an advanced control strategy for wind energy conversion systems that utilize doubly-fed induction generators (DFIGs). To overcome the inherent challenges of parameter sensitivity in conventional proportional-integral (PI) controllers and the practical drawbacks of mechanical speed sensors, a sophisticated sensorless control mechanism is developed. The core of the proposed system is an adaptive disturbance rejection controller enhanced with fuzzy logic and fractional-order mathematics. This configuration dynamically estimates the generator's rotational speed without requiring physical encoders, thereby reducing system cost and complexity. The controller is specifically designed to decouple and compensate for internal and external disturbances, including thermal-induced parameter drift and grid-side perturbations, without relying on feed-forward compensation loops. By employing fractional-order operators within the observer structure, the system achieves a higher degree of flexibility in gain tuning and transient response. Simulation results across diverse operational scenarios, such as fluctuating wind profiles and machine parameter variations, confirm that the proposed method effectively maintains precise speed tracking and robust disturbance rejection. A comparative analysis further illustrates that this hybrid approach offers superior dynamic performance and stability compared to traditional integer-order and non-adaptive control methods.

* Corresponding author.
E-mail address: sr.mosayyebi@iau.ac.ir.

1. Introduction

Wind energy is recognized as a clean, non-polluting, and economical source of power, making it an environmentally friendly alternative to conventional energy sources [1]. Its adoption is therefore increasing steadily. Modern wind power projects have reached significant scales, such that their influence on the performance and design of transmission networks is undeniable. Among various technologies, variable-speed wind turbines employing doubly-fed induction generators (DFIGs) offer numerous advantages, including improved power quality, reduced losses, and smaller electronic component sizes. These benefits contribute to lower production costs, enable power factor correction, and allow for the independent control of active and reactive power [2]. Consequently, DFIGs are widely regarded as the most suitable option for integrating wind turbines into the electrical grid, primarily due to the aforementioned features.

The most prevalent control strategy for the DFIG is vector control, which is typically implemented using proportional-integral (PI) controllers [3]. However, the performance of these controllers is highly dependent on accurate machine parameters, which are known to vary with temperature; consequently, thermal variations can significantly deteriorate the performance of conventional vector control methods [4]. Furthermore, PI controllers are inherently limited in their ability to handle the stochastic nature of wind speed. The two primary approaches to vector control are direct vector control (DVC) and indirect vector control (IVC) [5]. In DVC, decoupling between the d- and q-axis currents is achieved through feed-forward compensation. While this method is straightforward to implement, it tends to produce higher power fluctuations and greater harmonic distortion in the rotor and stator currents compared to IVC. In traditional IVC, the stator's active and reactive power are regulated by the rotor's direct- and quadrature-axis voltages (V_{dr} and V_{qr}), respectively. Similar to DVC, IVC also suffers from power oscillations and current harmonic distortion. To address these shortcomings, adaptive disturbance rejection control (ADRC) has been proposed as an effective solution [6]. A key advantage of ADRC is that it eliminates the need for feed-forward compensation [6]. The ADRC framework comprises three main components: a Tracking Differentiator (TD), a Non-Linear State Error Feedback (NLSEF) controller, and an Extended State Observer (ESO) [6]. This control strategy generates a control law that does not rely on an exact mathematical model of the system. Instead, it estimates and compensates for both internal disturbances (e.g., parameter variations) and external disturbances (e.g., sudden voltage dips, frequency deviations, and phase imbalances) in real time [7]. To date, conventional ADRC has been successfully applied to DFIG systems to address various challenges, including low-voltage ride through [8], maximum power point tracking [9], direct power control [10], power oscillation damping [11], voltage imbalance [12], stator voltage-oriented control [13], and voltage sag mitigation [14]. Despite its advantages, the traditional ADRC technique has several limitations. These include the requirement for a high bandwidth, which can introduce additional noise into the system [15]; a complex structure with numerous adjustable parameters [16]; and the introduction of an extended state that increases the system order, thereby adding to the complexity of the control algorithm [17].

In conventional vector control methods, the angular speed of the rotor shaft is measured using an encoder and subsequently utilized in control calculations. However, encoders present several disadvantages, including increased cost, additional cabling requirements, and the need for precise tuning [18]. In sensorless configurations, where the encoder is omitted, observers must be employed to estimate the rotor angular speed. The most commonly used observers include the model reference adaptive system (MRAS), Kalman filter (KF), extended Kalman filter (EKF), and sliding mode observer (SMO). Despite its popularity, the MRAS approach suffers from limitations such as sensitivity at low speeds and integrator drift. Moreover, since this observer is typically implemented in the stationary reference frame—where electrical quantities are sinusoidal functions of time—the design of controller parameters becomes challenging, and the observer may become inaccurate or even unstable in practice [19, 20]. The Kalman filter, on the other hand, assumes that noise is white and follows a Gaussian distribution, an assumption that is not always valid in machine drive systems. Additionally, the algorithm is computationally intensive, and the design of the estimator gain is complex, leading to prolonged

computation times and the need for high-speed processors [21, 22]. The extended Kalman filter was introduced to address some of these issues. However, its performance depends on accurate knowledge of the load torque, which increases computational burden and processing time. Further drawbacks of the EKF include the heavy computation of Jacobian matrices, biased estimation, a lack of analytical methods for selecting model covariances, sensitivity to round-off errors, and poor performance at low speeds, often resulting in instability due to linearization errors [19, 23, 24]. The SMO utilizes a high-frequency nonlinear switching function, which exacerbates system nonlinearity and complicates analysis and design. Another notable limitation of SMO is its sensitivity to machine parameter variations, particularly at low speeds [21, 23].

This paper addresses the aforementioned limitations of traditional vector control, conventional ADRC, and existing observer-based methods by implementing sensorless vector control of a DFIG using fuzzy fractional-order adaptive disturbance rejection control (FFADRC). In this approach, the coefficients of the NLSEF block are tuned using fuzzy logic, while the TD and ESO are designed with fractional-order dynamics. Furthermore, in the proposed fuzzy system, a linear combination of fractional-order derivatives of the block outputs is employed in place of the conventional error derivative. Based on this structure, the rotor speed is estimated directly from the FFADRC control laws and the disturbances estimated by the fractional-order ESO.

The remainder of this paper is organized as follows: Section 2 presents the structure and modeling of the wind energy conversion system (WECS). In Section 3, the concept of FFADRC is introduced. Section 4 details the FFADRC-based speed estimation and sensorless vector control for the rotor-side converter. Section 5 provides stability assessment using root locus technique. Section 6 describes the control strategy for the grid-side converter. Simulation results and discussion are presented in Section 7. Section 8 evaluates the robustness of FFADRC against internal and external disturbances. In Section 9, a comparative study of different ADRC variants is conducted. Finally, conclusion and future work are drawn in Section 10.

2. The Structure and Modeling of WECS

The topology of the WECS is illustrated in Fig. 1. The DFIG features windings on both its stationary and rotating parts, enabling bidirectional energy exchange between the shaft and the grid [25]. In this configuration, the stator is directly connected to the grid, while the rotor is interfaced through two converters to facilitate variable-speed operation. These converters, known as the rotor-side converter (RSC) and the grid-side converter (GSC), are arranged in a back-to-back topology. A DC-link capacitor is placed between them to mitigate voltage fluctuations. The RSC is responsible for torque control, speed regulation, and power factor control at the stator terminals, whereas the GSC maintains a constant DC-link voltage under varying operating conditions. The overall system performance depends not only on the DFIG itself but also on the control strategies applied to both converters [26]. Compared to other technologies, the use of a DFIG can increase energy capture by up to 30%, thereby reducing the overall cost of energy production [27]. In the following, the WECS model incorporating a DFIG is presented. First, the turbine model is introduced to establish the relationship between wind speed and the mechanical power extracted. Subsequently, the complete system model is described in detail.

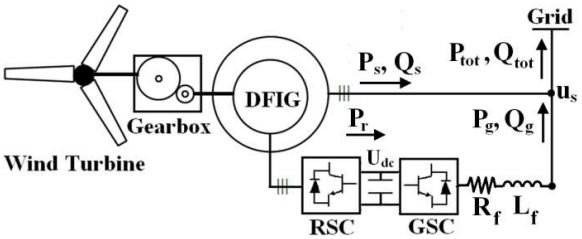

Fig. 1: Schematic diagram of the WECS incorporating a DFIG [28].

2.1. Wind Turbine Modeling

Wind energy is converted by the turbine into rotational force on the shaft. The resulting mechanical power output can be expressed as follows [29]:

$$P_m = \frac{1}{2}\rho\pi R_t^2 V_w^3 C_p(\lambda,\beta) \quad (1)$$

In this expression, ρ represents the air density, R_t is the rotor blade radius, V_w denotes the wind speed, λ is the tip speed ratio, and β is the blade pitch angle. The power coefficient, $C_p(\lambda,\beta)$, is defined as the ratio of the turbine's mechanical power output to the available

wind power. This coefficient determines the maximum power that can be extracted at a given wind speed. The relationship between the power coefficient, the blade pitch angle, and the tip speed ratio is expressed as follows [30]:

$$C_p(\lambda,\beta)=0.5176\left(\frac{116}{\lambda_i}-0.4\beta\right)e^{\left(-\frac{21}{\lambda_i}\right)}+(6.8e-3)\lambda_i \quad (2)$$

In this equation, e is Euler's number, and λ_i is a constant related to the structural parameters of the turbine blades, given by:

$$\frac{1}{\lambda_i}=\frac{1}{\lambda+0.8\beta}-\frac{(3.5e-2)}{\beta^3+1} \quad (3)$$

For optimal energy capture under low wind speed conditions, the blade pitch angle is regulated to zero. The tip speed ratio λ is then expressed as:

$$\lambda=\frac{R_t\omega_t}{V_w} \quad (4)$$

In this expression, R_t denotes the rotor blade radius, and ω_t represents the rotor angular velocity. The upper bound of the power coefficient C_p is defined by the Betz limit, with a theoretical maximum of 0.593.

2.2. Dynamic Modeling of the DFIG

In the synchronously rotating d-q reference frame, the stator and rotor voltage equations are given by the following set of equations [31]:

$$\begin{cases} v_{qs}=\dot{\lambda}_{qs}+\omega_s\lambda_{ds}+R_s i_{qs} \\ v_{ds}=\dot{\lambda}_{ds}-\omega_s\lambda_{qs}+R_s i_{ds} \\ v_{qr}=\dot{\lambda}_{qr}+\omega_r\lambda_{dr}+R_r i_{qr} \\ v_{dr}=\dot{\lambda}_{dr}-\omega_r\lambda_{qr}+R_r i_{dr} \end{cases} \quad (5)$$

where R_s and R_r are the stator and rotor resistances, respectively; i_{ds} and i_{qs} denote the d-q components of the stator current; and i_{dr} and i_{qr} represent the d-q components of the rotor current. The angular frequencies of the stator and rotor voltages and currents are given by ω_s and ω_r, respectively. The stator and rotor flux linkages are then expressed as follows:

$$\begin{cases} \lambda_{qs}=L_s i_{qs}+L_m i_{qr} \\ \lambda_{ds}=L_s i_{ds}+L_m i_{dr} \\ \lambda_{qr}=L_r i_{qr}+L_m i_{qs} \\ \lambda_{dr}=L_r i_{dr}+L_m i_{ds} \end{cases} \quad (6)$$

In these expressions, L_m denotes the magnetizing inductance, while L_r and L_s represent the rotor and stator inductances, respectively. The active and reactive power of the stator are given by:

$$\begin{cases} P_s=\frac{3}{2}\left(v_{ds}i_{ds}+v_{qs}i_{qs}\right) \\ Q_s=\frac{3}{2}\left(v_{qs}i_{ds}-v_{ds}i_{qs}\right) \end{cases} \quad (7)$$

Table 1 classifies the operating modes of the DFIG according to the direction of mechanical power, the active power flow in the stator and rotor, and the rotational speed of the generator.

Table 1: The operating mode of the DFIG [32]

Mode number	Working mode	Speed	Mechanical power	Stator power	Rotor power
1	motor	hyper-synchronous	deliver	receive	receive
2	generator	hyper-synchronous	receive	deliver	deliver
3	generator	sub-synchronous	receive	deliver	receive
4	motor	sub-synchronous	deliver	receive	deliver

2.3. Mechanical Part Modeling

The mechanical drivetrain of the wind turbine consists of a gearbox, a high-speed shaft, and a low-speed shaft. A comprehensive analysis of this subsystem is presented in [33]. In this study, a two-mass model is employed to represent the mechanical dynamics. The governing equation of this model is given by [34]:

$$\left(\frac{J_t}{N^2}+J_m\right)\dot{\omega}_m=T_m-T_{em}-f_v\omega_m \quad (8)$$

In this equation, N denotes the gearbox ratio, ω_m is the rotational speed of the DFIG (rad/s), and f_v represents the viscous friction coefficient (Nm). The mechanical torque of the DFIG is given by T_m (N·m), while T_{em} is the electromagnetic torque (N·m). The moments of inertia of the turbine and the DFIG are denoted by J_t and J_m, respectively, both expressed in kg.m².

2.4. Modeling of Back-to-Back PWM

This converter configuration enables bidirectional power flow between the rotor and the grid [35]. Fig. 2 illustrates the back-to-back converter topology, including the DC-link capacitor. The switching functions of the IGBTs are denoted by S_{mn}, where the subscript m identifies the converter arm and n

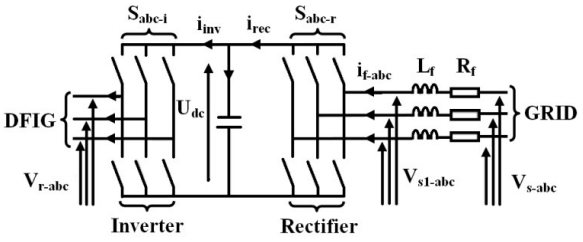

Fig. 2: Circuit topology of the back-to-back PWM converter [36].

indicates whether the switch belongs to the inverter or the rectifier. The variables i_f, i_{rec}, and i_{inv} represent the filter current, rectifier current, and inverter current, respectively. The governing equations of this system are given by [36]:

$$\begin{cases} C\dot{u}_{dc} = i_{rec} - i_{inv} \\ i_{rec} = \frac{3}{2}(s_{qr}I_{qf} + s_{dr}I_{df}) \\ L_f\dot{I}_{df} + R_fI_{df} + L_f\omega_sI_{qf} = V_{ds} - V_{ds1} \\ L_f\dot{I}_{qf} + R_fI_{qf} - L_f\omega_sI_{df} = V_{qs} - V_{qs1} \\ V_{ds1} = s_{dr}u_{dc} \\ V_{qs1} = s_{qr}u_{dc} \end{cases} \quad (9)$$

where C is the DC-link capacitance and u_{dc} is the voltage across it. The filter current is represented by its d-q components I_{df} and I_{qf}, while the grid voltage is given by V_{ds} and V_{qs}. The voltage at the filter-rectifier interface, denoted V_{s1}, is resolved into its d-q components $V_{ds1}$and V_{qs1}. The parameters R_f, L_f, and I_f correspond to the filter resistance, inductance, and current, respectively. Furthermore, s_{dr} and s_{qr} are the modulation indices.

3. Fuzzy Fractional-order Adaptive Disturbance Rejection Control (FFADRC)

The coefficients of PI controllers must be carefully tuned according to the machine parameters to ensure an optimal dynamic response. Nevertheless, these parameters are susceptible to change under varying environmental and operational conditions. For example, resistance is affected by temperature, and inductance is influenced by saturation. Furthermore, PI controllers do not perform adequately in wind turbine systems when subjected to sudden wind variations. To overcome the impact of internal uncertainties and external disturbances, Dr. Han proposed ADRC, a method based on the ESO [37]. ADRC is a robust control technique that has been shown to serve as a suitable replacement for the PI controller. By employing feed-forward compensation to inject the total disturbance (both internal and external) into the system input, the overall system is transformed into a simple integrator or a linear system [38]. Consider an n-order single-input single-output (SISO) nonlinear system of the following form [6]:

$$y^{(n)}(t) = f(y(t), y^{(1)}(t), y^{(2)}(t),..., y^{(n-1)}(t), d(t), u(t)) + b_0u(t) \quad (10)$$

This can be written as:

$$\begin{cases} \dot{x}_1(t) = x_2(t) \\ \dot{x}_2(t) = x_3(t) \\ \vdots \\ \dot{x}_n(t) = f(x_1(t), x_2(t),...,d(t)) + b_0u(t) \\ y(t) = x_1(t) \end{cases} \quad (11)$$

where $y(t)$ is the system output, $u(t)$ is the control input, $d(t)$ represents external disturbances, $f(\cdot)$ denotes the total disturbance (comprising both internal uncertainties and external disturbances), and b_0 is a known system parameter. As previously discussed, ADRC consists of three main components, which are illustrated in Fig. 3. For the system described above, these components are as follows:

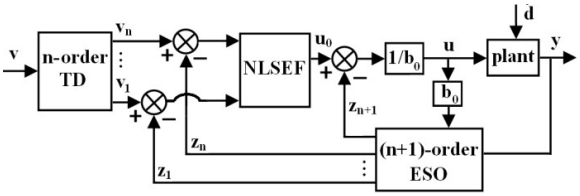

Fig. 3: Schematic representation of the ADRC framework applied to an n-order nonlinear SISO system [6, 11].

(a) n-order nonlinear TD, described by the following equations:

$$\begin{cases} \dot{v}_1(t) = v_2(t) \\ \dot{v}_2(t) = v_3(t) \\ \vdots \\ \dot{v}_{n-1}(t) = v_n(t) \\ \dot{v}_n(t) = R^n.\psi\left(v_1(t) - v(t), \frac{v_2(t)}{R},...,\frac{v_n(t)}{R^{n-1}}\right), \ \psi(0,0,...,0) = 0 \end{cases} \quad (12)$$

In these equations, $v_1(t)$ denotes the tracking signal of the reference input $v(t)$, while $v_2(t),\ldots,v_n(t)$ are the higher-order derivatives of $v_1(t)$. The parameter R (R>0) is a tuning constant, and $\psi(\cdot)$ is a suitably chosen nonlinear function.

(b) (n+1)-order nonlinear ESO, given by:

$$\begin{cases} \dot{z}_1(t) = z_2(t) + \beta_1 g_1(y(t) - z_1(t)) \\ \dot{z}_2(t) = z_3(t) + \beta_2 g_2(y(t) - z_1(t)) \\ \vdots \\ \dot{z}_n(t) = z_{n+1}(t) + \beta_n g_n(y(t) - z_1(t)) + b_0 u(t) \\ \dot{z}_{n+1}(t) = \beta_{n+1} g_{n+1}(y(t) - z_1(t)) \end{cases} \quad (13)$$

where $u(t)$ denotes the system input. The observer gains are represented by β_i (i=1, 2, …, n+1), and g_i (i=1, 2, …, n+1) are suitably defined nonlinear functions. The variable $z_1(t)$ tracks the system output $y(t)$, with $z_2(t)$, …, $z_n(t)$ being its higher-order derivatives. The extended state $z_{n+1}(t)$ estimates the total disturbance. The parameter b_0 is as previously defined. The purpose of the ESO is to enable the estimated states z_i (i=1, 2, …, n) to converge to the actual system states x_i and for z_{n+1} to accurately estimate the total disturbance, achieved by appropriately selecting the nonlinear functions g_i and adjusting the gains β_i.

(c) NLSEF, responsible for generating the ADRC control law expressed as:

$$u(t) = \frac{1}{b_0}\left(\psi(z(t) - v(t)) - z_{n+1}(t)\right) \quad (14)$$

where $z(t)$ and $v(t)$ are vectors defined as $z(t)=(z_1(t), z_2(t), \ldots, z_n(t))$ and $v(t)=(v_1(t), v_2(t), \ldots, v_n(t))$, respectively. To obtain an optimal and rapid control performance in a second-order SISO nonlinear system, the ADRC blocks are formulated as follows [6, 37]:

$$\begin{cases} \boldsymbol{TD}: & \begin{cases} \dot{v}_1 = v_2 \\ \dot{v}_2 = -r.\mathrm{sgn}\left(v_1(t) - v(t) + \dfrac{v_2(t)|v_2(t)|}{2r}\right) \end{cases} \\ \boldsymbol{ESO}: & \begin{cases} \dot{z}_1(t) = z_2(t) - \beta_1(z_1(t) - y(t)) \\ \dot{z}_2(t) = z_3(t) - \beta_2 fal(z_1(t) - y(t), 0.5, \delta) + b_0 u(t) \\ \dot{z}_3(t) = -\beta_3 fal(z_1(t) - y(t), 0.25, \delta) \end{cases} \\ \boldsymbol{NLSEF}: & \begin{cases} e_1 = v_1 - z_1, \quad e_2 = v_2 - z_2 = \dot{e}_1 \\ \mathbf{u_0} = k_p fal(e_1, \alpha_1, \delta_1) + k_d fal(e_2, \alpha_2, \delta_2) \end{cases} \\ \boldsymbol{control\_law}: & u(t) = \dfrac{1}{b}\left(u_0(t) - z_3(t)\right) \end{cases} \quad (15)$$

The parameter r is a positive constant that governs the tracking speed, while sgn denotes the sign function. The coefficients k_p and k_d correspond to the proportional and derivative terms, respectively. The remaining parameters, namely α_1, δ_1, α_2, δ_2, and δ, are ADRC parameters that require specification. The function $fal(\cdot)$ is defined according to [6, 11, 37]:

$$fal(e, \alpha, \delta) = \begin{cases} |e|^{\alpha}\,\mathrm{sgn}(e) & |e| > \delta \\ \dfrac{e}{\delta^{1-\alpha}} & |e| \le \delta \end{cases} \quad (16)$$

In the case where α<1, $fal(e, \alpha, \delta)$ behaves such that large errors are attenuated with a small gain, while small errors are amplified with a large gain.

The conventional ADRC structure involves a large number of parameters that must be tuned. To mitigate this drawback, a linear version of ADRC has been introduced, offering satisfactory results in comparison to nonlinear ADRC [39]. In this linear formulation, the ESO and NLSEF are replaced by their linear equivalents, namely the linear extended state observer (LESO) and linear state error feedback (LSEF), which are described by the following equations:

$$\begin{cases} \boldsymbol{LSEF}: \mathbf{u_0} = k_p e_1 + k_d E_2 \\ \boldsymbol{LESO}: \begin{cases} \dot{z}_1(t) = z_2(t) - \beta_1(z_1(t) - y(t)) \\ \dot{z}_2(t) = z_3(t) - \beta_2(z_1(t) - y(t)) + b_0 u(t) \\ \dot{z}_3(t) = -\beta_3(z_1(t) - y(t)) \end{cases} \end{cases} \quad (17)$$

Fig. 4 demonstrates that the tuning of k_p and k_d significantly influences system behavior [40]. A larger k_p reduces transient time and enhances tracking precision but increases overshoot, compromising dynamic performance. Likewise, a higher k_d boosts response speed while introducing sensitivity to high-frequency noise. To resolve this conflict, fuzzy logic is adopted to determine the optimal LSEF coefficients, as illustrated in Fig. 5. The associated fuzzy rules, detailed in Table 2, are constructed using the error signals e_1 and E_2, with the following linguistic classifications: "*NeBi*" (Negative Big), "*NeMe*" (Negative Medium), "*NeSm*" (Negative Small), "*Zer*" (Zero), "*PoSm*" (Positive Small), "*PoMe*" (Positive Medium), and "*PoBi*" (Positive Big).

Table 2: Fuzzy rule base for tuning k_p and k_d (corresponding to Fig. 5)

E_2 \ e_1	NeBi	NeMe	NeSm	Zer	PoSm	PoMe	PoBi
NeBi	PoBi	PoMe	PoMe	PoMe	PoSm	PoSm	Zer
NeMe	PoMe	PoMe	PoMe	PoSm	PoSm	Zer	NeSm
NeSm	PoMe	PoMe	PoSm	PoSm	Zer	NeSm	NeSm
Zer	PoMe	PoSm	PoSm	Zer	NeSm	NeSm	NeMe
PoSm	PoSm	PoSm	Zer	NeSm	NeSm	NeMe	NeMe
PoMe	PoSm	Zer	NeSm	NeSm	NeMe	NeMe	NeMe
PoBi	Zer	NeSm	NeSm	NeMe	NeMe	NeMe	NeBi

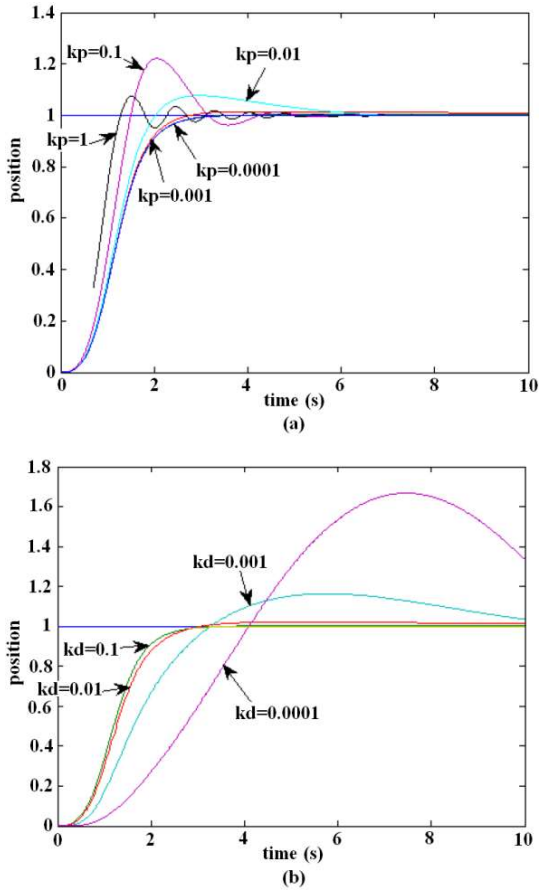

Fig. 4: Dynamic response of the system under variations of (a) k_p and (b) k_d [40].

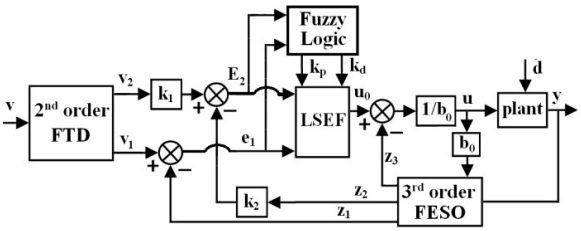

Fig. 5: The proposed fuzzy fractional-order ADRC scheme.

Referring to Fig. 5, the conventional error derivative $e_2=v_2-z_2$ is substituted with the linear combination $E_2=k_1v_2-k_2z_2$. This modification not only improves the performance and controllability of the ADRC but also expands its degrees of freedom. Additionally, leveraging the benefits of fractional-order calculus, the extended state observer and tracking differentiator are realized as fractional-order ESO (FESO) and fractional-order TD (FTD), respectively.

Fractional-order calculations rely on extending the concepts of integration and differentiation to non-integer orders. The corresponding integral-derivative operator is given by [41]:

$$ {}_aD_t^{\alpha} = \begin{cases} \dfrac{d^{\alpha}}{dt^{\alpha}} & \mathrm{Re}[\alpha] > 0 \\ 1 & \mathrm{Re}[\alpha] = 0 \\ \displaystyle\int_a^t (d\tau)^{-\alpha} & \mathrm{Re}[\alpha] < 0 \end{cases} \tag{18} $$

where α is the order of the fractional integral-derivative operator. Consider a second-order SISO nonlinear fractional-order system with commensurate order α, as illustrated in Fig. 5. Its dynamics are represented by the following differential equation:

$$ \boldsymbol{y}^{(2\alpha)} = \boldsymbol{f}(\boldsymbol{y}^{(\alpha)}, \boldsymbol{y}, \boldsymbol{d}, \boldsymbol{u}) + \boldsymbol{b}_0\boldsymbol{u} \tag{19} $$

Let the system states be chosen as $x_1=y$ and $x_2=y^{(\alpha)}$, and the extended state as $x_3=f(y^{(\alpha)}, y, d, u)$. The corresponding state-space model is then expressed as:

$$ \begin{cases} \boldsymbol{x}^{(\alpha)} = \boldsymbol{A}\boldsymbol{x} + \boldsymbol{B}\boldsymbol{u} + \boldsymbol{E}\boldsymbol{h} \\ \boldsymbol{y} = \boldsymbol{C}\boldsymbol{x} \end{cases} \tag{20} $$

where $\boldsymbol{x} = \begin{bmatrix} x_1 \\ x_2 \\ x_3 \end{bmatrix}$, $\boldsymbol{x}^{(\alpha)} = \begin{bmatrix} x_1^{(\alpha)} \\ x_2^{(\alpha)} \\ x_3^{(\alpha)} \end{bmatrix}$, $\boldsymbol{A} = \begin{bmatrix} 0 & 1 & 0 \\ 0 & 0 & 1 \\ 0 & 0 & 0 \end{bmatrix}$, $\boldsymbol{B} = \begin{bmatrix} 0 \\ b_0 \\ 0 \end{bmatrix}$, $\boldsymbol{C} = \begin{bmatrix} 1 & 0 & 0 \end{bmatrix}$, $\boldsymbol{E} = \begin{bmatrix} 0 \\ 0 \\ 1 \end{bmatrix}$ and $\boldsymbol{h} = \boldsymbol{f}^{(\alpha)}(\bullet)$.

To estimate the states x_1, x_2, and the extended state x_3, a linear FESO is formulated as follows:

$$ \begin{cases} \boldsymbol{z}^{(\alpha)} = \boldsymbol{A}\boldsymbol{z} + \hat{\boldsymbol{B}}\boldsymbol{u} + \boldsymbol{L}(\boldsymbol{y} - \hat{\boldsymbol{y}}) \\ \hat{\boldsymbol{y}} = \boldsymbol{C}\boldsymbol{z} \end{cases} \tag{21} $$

where $\boldsymbol{z} = \begin{bmatrix} z_1 \\ z_2 \\ z_3 \end{bmatrix}$, $\boldsymbol{z}^{(\alpha)} = \begin{bmatrix} z_1^{(\alpha)} \\ z_2^{(\alpha)} \\ z_3^{(\alpha)} \end{bmatrix}$, $\hat{\boldsymbol{B}} = \begin{bmatrix} 0 \\ \hat{b}_0 \\ 0 \end{bmatrix}$, and $\boldsymbol{L} = \begin{bmatrix} \beta_1 \\ \beta_2 \\ \beta_3 \end{bmatrix}$ is observer gain. The variables z_1, z_2, and z_3 in the above expression represent the estimated values of x_1, x_2, and x_3, respectively. Furthermore, $\hat{\boldsymbol{b}}_0$ is the estimate of the system parameter b_0. Eq. 21 can then be written as:

$$ \begin{bmatrix} z_1^{(\alpha)} \\ z_2^{(\alpha)} \\ z_3^{(\alpha)} \end{bmatrix} = \underbrace{\begin{bmatrix} -\beta_1 & 1 & 0 \\ -\beta_2 & 0 & 1 \\ -\beta_3 & 0 & 0 \end{bmatrix}}_{(A-LC)} \begin{bmatrix} z_1 \\ z_2 \\ z_3 \end{bmatrix} + \underbrace{\begin{bmatrix} 0 \\ \hat{b} \\ 0 \end{bmatrix}}_{\hat{B}} \boldsymbol{u} + \underbrace{\begin{bmatrix} \beta_1 \\ \beta_2 \\ \beta_3 \end{bmatrix}}_{L} \boldsymbol{y} \tag{22} $$

The characteristic equation of the FESO is expressed as:

$$ \det(\boldsymbol{sI} - (\boldsymbol{A} - \boldsymbol{LC})) = \boldsymbol{s}^3 + \beta_1\boldsymbol{s}^2 + \beta_2\boldsymbol{s} + \beta_3 \tag{23} $$

The observer stability is guaranteed by placing the poles of its characteristic equation at $-\omega_0$, with ω_0 representing the observer bandwidth [38]. Thus,

$$\begin{aligned} &s^3+\beta_1 s^2+\beta_2 s+\beta_3=(s+\omega_o)^3 \\ &\Rightarrow \beta_1=3\omega_o,\ \beta_2=3\omega_o^2,\ \beta_3=\omega_o^3 \end{aligned} \tag{24}$$

The observer bandwidth ω_0 directly influences the FESO performance: a higher value accelerates state estimation but may degrade dynamic stability. Hence, ω_0 must be carefully selected to balance speed and stability. A well-designed FESO ensures precise tracking of the extended state. As discussed previously, adopting the control law $u=\frac{u_0-z_3}{b_0}$ simplifies the system to an integrator of the form $y^{(2\alpha)}\approx u_0$. For the second-order FTD illustrated in Fig. 5, the governing equations are [42]:

$$\begin{cases} v_1^{(\alpha)}=v_2 \\ v_2^{(\alpha)}=-r.\mathrm{sgn}\left(v_1-v+\dfrac{\Gamma^2(\alpha+1)}{r.\Gamma(2\alpha+1)}v_2|v_2|\right) \end{cases} \tag{25}$$

Where $\Gamma(\cdot)$ denotes the Gamma function.

4. FFADRC-based Speed Estimation and Sensorless Vector Control for the RSC

Given the drawbacks of conventional ADRC discussed earlier, and recognizing the significance of tuning the LSEF block coefficients as well as the proper design of the ESO and TD, the sensorless vector control of the RSC is implemented using FFADRC in this section. The proposed method integrates fuzzy logic with fractional-order control. The rotor speed is estimated based on the FFADRC control laws and the disturbances estimated by the FESO. According to Eqs. 5 and 6, the stator flux derivatives in the d- and q-axis directions are:

$$\begin{cases} \dfrac{d\lambda_{qs}}{dt}=v_{qs}-\dfrac{R_s}{L_s}\lambda_{qs}-\omega_s\lambda_{ds}+\dfrac{R_sL_m}{L_s}i_{qr} \\ \dfrac{d\lambda_{ds}}{dt}=v_{ds}-\dfrac{R_s}{L_s}\lambda_{ds}+\omega_s\lambda_{qs}+\dfrac{R_sL_m}{L_s}i_{dr} \end{cases} \tag{26}$$

By employing Eq. 6 and introducing the leakage factor, $\sigma=1-\frac{L_m^2}{L_sL_r}$, the rotor fluxes in the d-q reference frame are obtained as:

$$\begin{cases} \lambda_{qr}=\dfrac{L_m}{L_s}\lambda_{qs}+\sigma L_r i_{qr} \\ \lambda_{dr}=\dfrac{L_m}{L_s}\lambda_{ds}+\sigma L_r i_{dr} \end{cases} \tag{27}$$

The rotor fluxes can be derived from Eq. 26 and the differentiation of Eq. 27, yielding:

$$\begin{cases} \dfrac{d\lambda_{qr}}{dt}=\dfrac{L_m}{L_s}v_{qs}-\dfrac{R_sL_m}{L_s^2}\lambda_{qs}-\dfrac{L_m}{L_s}\omega_s\lambda_{ds}+\dfrac{R_sL_m^2}{L_s^2}i_{qr}+\sigma L_r\dfrac{di_{qr}}{dt} \\ \dfrac{d\lambda_{dr}}{dt}=\dfrac{L_m}{L_s}v_{ds}-\dfrac{R_sL_m}{L_s^2}\lambda_{ds}+\dfrac{L_m}{L_s}\omega_s\lambda_{qs}+\dfrac{R_sL_m^2}{L_s^2}i_{dr}+\sigma L_r\dfrac{di_{dr}}{dt} \end{cases} \tag{28}$$

Substituting (28) into (6) yields the following expressions for the derivatives of the rotor and stator currents:

$$\begin{cases} \dfrac{di_{qr}}{dt}=\dfrac{v_{qr}}{\sigma L_r}-\dfrac{1}{\sigma L_r}\left(R_r+R_s\dfrac{L_m^2}{L_s^2}\right)i_{qr}-\dfrac{\omega_r\lambda_{dr}}{\sigma L_r} \\ \qquad -\dfrac{L_m}{\sigma L_sL_r}v_{qs}+\dfrac{R_sL_m}{\sigma L_s^2L_r}\lambda_{qs}+\dfrac{L_m\omega_s}{\sigma L_sL_r}\lambda_{ds} \\ \dfrac{di_{dr}}{dt}=\dfrac{v_{dr}}{\sigma L_r}-\dfrac{1}{\sigma L_r}\left(R_r+R_s\dfrac{L_m^2}{L_s^2}\right)i_{dr}+\dfrac{\omega_r\lambda_{qr}}{\sigma L_r} \\ \qquad -\dfrac{L_m}{\sigma L_sL_r}v_{ds}+\dfrac{R_sL_m}{\sigma L_s^2L_r}\lambda_{ds}-\dfrac{L_m\omega_s}{\sigma L_sL_r}\lambda_{qs} \end{cases} \tag{29}$$

In the stator flux-oriented (SFO) reference frame, the stator flux is aligned with the d-axis, implying that its q-axis component is zero (λ_{qs}=0) and the d-axis flux is constant ($\lambda_{ds}=\lambda_s\Rightarrow\frac{d\lambda_{ds}}{dt}=0$). Consequently, from Eq. 6, the stator current and rotor flux expressions in the d-q frame are given by:

$$\begin{cases} i_{ds}=\dfrac{\lambda_{ds}-L_mi_{dr}}{L_s}, & i_{qs}=-\dfrac{L_m}{L_s}i_{qr} \\ \lambda_{dr}=\dfrac{L_m}{L_s}\lambda_{ds}+\sigma L_ri_{dr}, & \lambda_{qr}=\sigma L_ri_{qr} \end{cases} \tag{30}$$

Under stator flux orientation and assuming negligible stator resistance, the stator voltage equations reduce to v_{ds}=0 and $v_{qs}=\omega_s\lambda_{ds}$. Consequently, Eq. 29 can be simplified as follows:

$$\begin{cases} \dfrac{di_{qr}}{dt}=\dfrac{v_{qr}}{\sigma L_r}-\dfrac{R_r}{\sigma L_r}i_{qr}-\omega_r\left(\dfrac{L_m}{\sigma L_sL_r}\lambda_s+i_{dr}\right) \\ \dfrac{di_{dr}}{dt}=\dfrac{v_{dr}}{\sigma L_r}-\dfrac{R_r}{\sigma L_r}i_{dr}+\omega_ri_{qr} \end{cases} \tag{31}$$

Differentiating Eq. 31 yields:

$$\begin{cases} \dfrac{d^2 y_q(t)}{dt^2} = b_o u_q(t) + f_{3q} \\ \dfrac{d^2 y_d(t)}{dt^2} = b_o u_d(t) + f_{3d} \\ b_0 = -\dfrac{R_r}{\sigma^2 L_r^2} \end{cases} \quad (32)$$

In these expressions, $y_q(t)=i_{qr}(t)$ and $y_d(t)=i_{dr}(t)$ denote the rotor-side outputs provided to the observers. The FFADRC generates control signals $u_q(t)=v_{qr}(t)$ and $u_d(t)=v_{dr}(t)$, which are applied to the RSC. The quantities f_{3d} and f_{3q} are the total disturbances (internal and external) estimated by the observers, and their expressions are as follows:

$$\begin{cases} f_{3q} = -\dfrac{\omega_r}{\sigma L_r} v_{dr} + \dfrac{1}{\sigma L_r}\dfrac{dv_{qr}}{dt} + \left(\dfrac{R_r^2}{\sigma^2 L_r^2} - \omega_r{}^2\right) i_{qr} \\ \quad + \dfrac{2R_r \omega_r i_{dr}}{\sigma L_r} + \dfrac{R_r L_m \omega_r \lambda_s}{\sigma^2 L_s L_r^2} \\ f_{3d} = +\dfrac{\omega_r}{\sigma L_r} v_{qr} + \dfrac{1}{\sigma L_r}\dfrac{dv_{dr}}{dt} + \left(\dfrac{R_r^2}{\sigma^2 L_r^2} - \omega_r{}^2\right) i_{dr} \\ \quad - \dfrac{2R_r \omega_r i_{qr}}{\sigma L_r} - \dfrac{L_m \omega_r{}^2 \lambda_s}{\sigma L_s L_r} \end{cases} \quad (33)$$

The proposed strategy is depicted in Fig. 6. By employing third-order observers, the disturbance estimates satisfy $z_{3d}=f_{3d}$ and $z_{3q}=f_{3q}$. Eq. 33 then leads to the following expression:

$$-L_m \lambda_s i_{qr} \omega_r{}^2 + \left(L_s\left(v_{qr} i_{qr} + v_{dr} i_{dr} - 2R_r\left(i_{dr}^2 + i_{qr}^2\right)\right) - \frac{R_r L_m i_{dr} \lambda_s}{\sigma L_r}\right)\omega_r + L_s\left(i_{qr}\frac{dv_{dr}}{dt} - i_{dr}\frac{dv_{qr}}{dt}\right) + \sigma L_s L_r\left(z_{3q} i_{dr} - z_{3d} i_{qr}\right) = 0 \quad (34)$$

Based on the relation $\omega_s-\omega_m=\omega_r$, the estimated rotor electrical speed ($\hat{\omega}_m$) is given by Eq. 35.

Eq. 35 forms the basis of the rotor speed estimation. Referring to Fig. 6, two FFADRCs are configured in the synchronous dq reference frame. Their output voltages, v_{dr} and v_{qr}, are transformed to the rotor DQ frame and then converted to three-phase quantities for the PWM modulator. The angle θ_r of the rotor voltage space vector, required for the dq-to-DQ transformation, is derived by subtracting the estimated rotor angle ($\hat{\theta}_m$) from the stator voltage space vector angle θ_s. The three-phase rotor currents are likewise transformed into the dq frame and fed into the FFADRCs. As the controllers process rotor currents referred to the stator side, a conversion to the rotor side is applied before PWM signal generation using the turns ratio $u=N_s/N_r$, where N_s and N_r are the stator and rotor turns per phase, respectively.

Since the design procedure for the d- and q-axis controllers is identical, only the d-axis controller design is presented here. The observer is designed according to Eq. 21, requiring only the determination of the observer bandwidth ω_0. The resulting FFADRC control law is given by:

$$\begin{cases} e_{1d} = v_{1dr} - z_{1d} \\ e_{2d} = k_{1d}.v_{2dr} - k_{2d}.z_{2d} = k_{1d}.v_{1dr}^{(\alpha)} - k_{2d}.z_{1d}^{(\alpha)} \\ v_{dr-0} = k_p.e_{1d} + k_d.e_{2d} \end{cases} \quad (36)$$

where α denotes the fractional order, with $v_{2dr}=v_{1dr}^{(\alpha)}$ and $z_{2d}=z_{1d}^{(\alpha)}$. The coefficients k_p and k_d are tuned via fuzzy logic, as mentioned earlier. Using the feed-forward configuration, the FFADRC output is expressed as:

$$v_{dr} = v_{dr-0} - \frac{z_{3d}}{b_0} = v_{dr-0} + \left(\frac{\sigma^2 L_r^2}{R_r}\right) z_{3d} \quad (37)$$

Using the observer, the extended state z_{3d} is estimated. The stator fluxes in the $\alpha\beta$ reference frame are described by the following equations [43]:

$$\begin{cases} \lambda_{\alpha s} = \int (v_{\alpha s} - R_s i_{\alpha s})dt \\ \lambda_{\beta s} = \int (v_{\beta s} - R_s i_{\beta s})dt \end{cases} \quad (38)$$

where $v_{\alpha s}$ and $v_{\beta s}$ are the stator voltage components in the $\alpha\beta$ reference frame, and $i_{\alpha s}$ and $i_{\beta s}$ are the corresponding stator current components. Eq.39 provides the basis for calculating the stator flux amplitude and the stator voltage space vector angle within the flux observer block.

$$\begin{cases} \lambda_s = \sqrt{\lambda_{\alpha s}^2 + \lambda_{\beta s}^2} \\ \theta_s = \tan^{-1}\left(\dfrac{\lambda_{\beta s}}{\lambda_{\alpha s}}\right) \end{cases} \quad (39)$$

Applying Eqs. 7 and 30 under the SFO condition, the stator reactive power can be derived as:

$$\hat{\omega}_m = \omega_s - \left(\frac{-L_s\left(v_{qr} i_{qr} + v_{dr} i_{dr} - 2R_r\left(i_{dr}^2 + i_{qr}^2\right)\right) + \frac{R_r L_m i_{dr} \lambda_s}{\sigma L_r} \pm \sqrt{\left(L_s\left(v_{qr} i_{qr} + v_{dr} i_{dr} - 2R_r\left(i_{dr}^2 + i_{qr}^2\right)\right) - \frac{R_r L_m i_{dr} \lambda_s}{\sigma L_r}\right)^2 + 4L_m \lambda_s i_{qr}\left(L_s\left(i_{qr}\frac{dv_{dr}}{dt} - i_{dr}\frac{dv_{qr}}{dt}\right) + \sigma L_s L_r\left(z_{3q} i_{dr} - z_{3d} i_{qr}\right)\right)}}{-2L_m \lambda_s i_{qr}} \right) \quad (35)$$

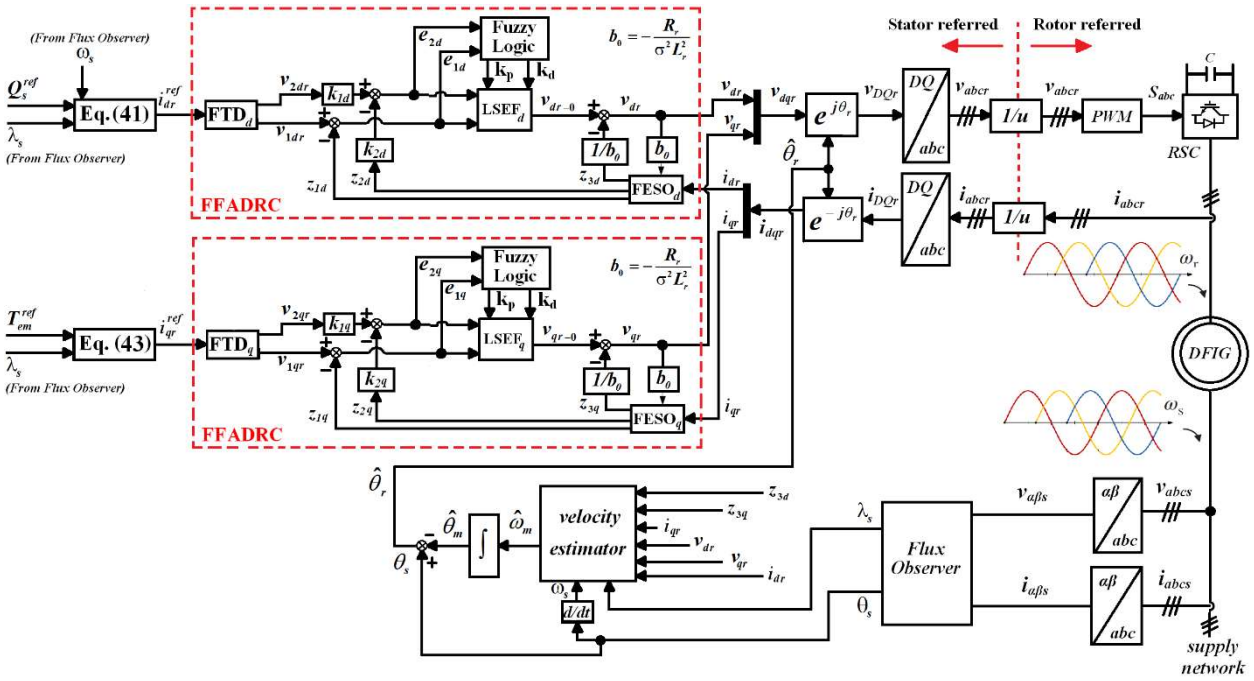

Fig. 6: FFADRC-based speed estimation and sensorless vector control for the RSC.

$$Q_s = \frac{3}{2}\left(v_{qs}\cdot \underbrace{\frac{1}{L_s}\left(\lambda_{ds} - L_m i_{dr}\right)}_{i_{ds}} - \underbrace{v_{ds}}_{\cong 0} i_{qs} \right) = \frac{3 v_{qs}}{2 L_s}\left(\lambda_{ds} - L_m i_{dr}\right) = \frac{3\omega_s \lambda_s}{2 L_s}\left(\lambda_s - L_m i_{dr}\right) \quad (40)$$

Consequently, the d-component of the rotor reference current is expressed as:

$$i_{dr}^{ref} = \frac{1}{L_m}\left(\lambda_s - \frac{2}{3}\frac{L_s}{\omega_s \lambda_s} Q_s^{ref}\right) \quad (41)$$

According to [43] and under the SFO condition, the electromagnetic torque is given by:

$$T_{em} = \frac{3}{2} p \frac{L_m}{L_s}\left(\underbrace{\lambda_{qs}}_{\cong 0} i_{dr} - \lambda_{ds} i_{qr} \right) = -\frac{3}{2} p \frac{L_m}{L_s} \lambda_s i_{qr} \quad (42)$$

From the above, the q-component of the rotor reference current is derived as:

$$i_{qr}^{ref} = -\frac{2}{3}\frac{L_s}{p L_m \lambda_s} T_{em}^{ref} \quad (43)$$

where p represents the number of pole pairs. As can be seen from Fig. 6, the LSEF receives a linear combination of the FTD and FESO outputs. Because the FFADRC structure is symmetric for the d and q axes, the effect of this combination is described only for the d-axis, as follows:

As previously discussed, for a second-order linear fractional-order system controlled by FFADRC, the relationship $y^{(2\alpha)} \approx u_0$ holds, where $u_0 = k_p(v_1 - z_1) + k_d(v_1^{(\alpha)} - z_1^{(\alpha)})$ (with α being the fractional order), so $y^{(2\alpha)} = k_p(v_1 - z_1) + k_d(v_1^{(\alpha)} - z_1^{(\alpha)})$. Consequently, the following equation is established for the FFADRC in Fig. 6:

$$\begin{aligned} i_{dr}^{(2\alpha)} &= k_p(v_{1dr} - z_{1d}) + k_d(k_{1d} v_{2dr} - k_{2d} z_{2d}) \\ &= k_p(v_{1dr} - z_{1d}) + k_d(k_{1d} v_{1dr}^{(\alpha)} - k_{2d} z_{1d}^{(\alpha)}) \end{aligned} \quad (44)$$

Because z_{1d} estimates i_{dr} and v_{1dr} estimates i_{dr}^{ref}, the following relationship holds:

$$i_{dr}^{(2\alpha)} = k_p(i_{dr}^{ref} - i_{dr}) + k_d(k_{1d} i_{dr}^{ref(\alpha)} - k_{2d} i_{dr}^{(\alpha)}) \quad (45)$$

The closed-loop transfer function of the DFIG rotor with FFADRC is derived via the Laplace transform and can be expressed as:

$$\frac{i_{dr}(s)}{i_{dr}^{ref}(s)} = \frac{k_d k_{1d} s^{(\alpha)} + k_p}{s^{(2\alpha)} + k_d k_{2d} s^{(\alpha)} + k_p} \quad (46)$$

The corresponding equivalent circuit is shown in Fig. 7.

5. Stability Assessment Using Root Locus Technique

A commensurate fractional-order system is described by the following transfer function [41]:

$$G(s) = K\frac{B(s^\alpha)}{A(s^\alpha)} = K\frac{\sum_{k'=0}^{m} b_{k'}(s^\alpha)^{k'}}{\sum_{k=0}^{n} a_k (s^\alpha)^k} \quad (47)$$

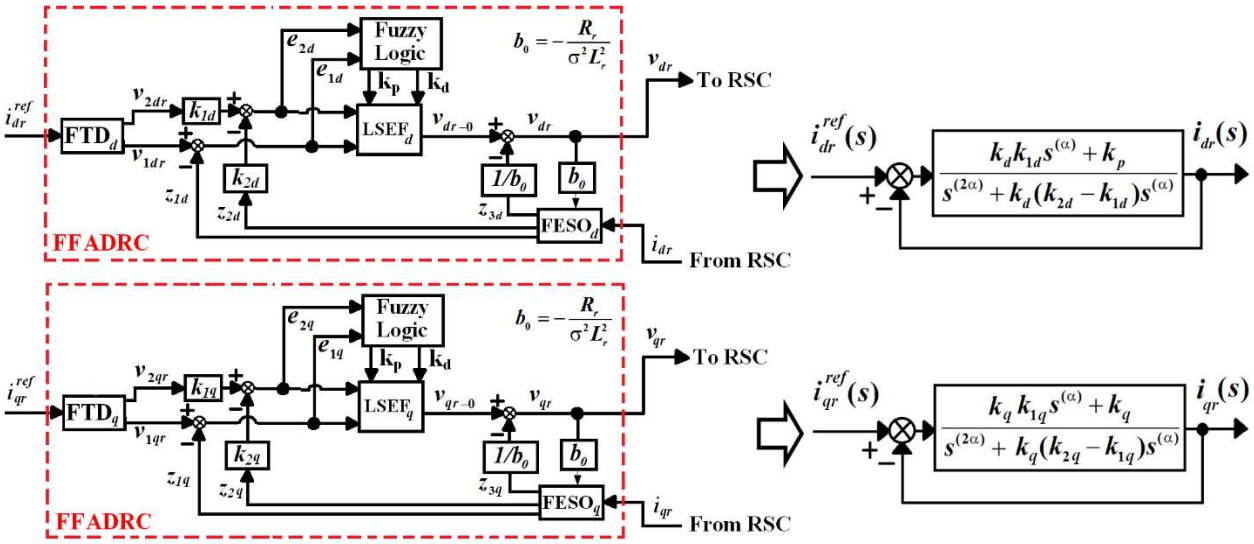

Fig. 7: Equivalent circuit of rotor current control in DFIG using FFADRC.

where $0<\alpha<1$, $k, k' \in Z$, a_k and b_k denote time-invariant coefficients, while K represents the gain. From Eq. 47, the characteristic polynomial takes the following form:

$$D(s) = a_n s^{n\alpha} + a_{n-1} s^{(n-1)\alpha} + \ldots + a_1 s^{\alpha} + a_0 \quad (48)$$

With the substitution $w=s^{\alpha}$, the characteristic polynomial becomes:

$$D(z) = a_n z^{n} + a_{n-1} z^{(n-1)} + \ldots + a_1 z + a_0 \quad (49)$$

Let z_i (i=1, 2, …, n) denote the roots of Eq. 49. The system is stable if and only if $|\arg(z_i)| > \frac{\alpha\pi}{2}$ holds for every i. Fig. 8 depicts the corresponding stable and unstable regions.

When the proportional and derivative gains in Eq. 46 are set to $k_p=\omega_c^2$ and $k_d=2\omega_c$ (with ω_c representing the controller bandwidth), the characteristic equation yields roots exclusively in the left half-plane for all positive k_{2d}, confirming unconditional stability. The effects of the individual coefficients k_{1d}, k_{2d}, ω_c, and α on stability will be examined separately.

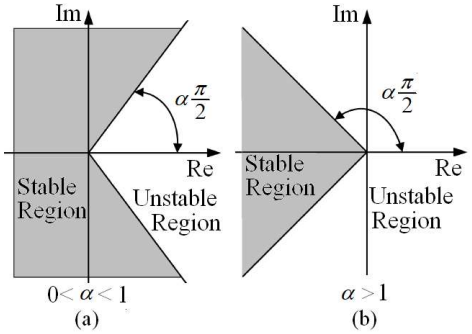

Fig. 8: Stability regions for a fractional-order system of commensurate order α: (a) $0<\alpha<1$, (b) $\alpha>1$ [41].

5.1. Dependence of Stability on k_{1d} and k_{2d}

With ω_c=10, α=0.7, and k_{2d}=1, the root locus is generated for a range of k_{1d} values and displayed in Fig. 9. The stability boundary, marked by the red line, is defined by $|\theta| = \frac{0.7\pi}{2}$. From Fig. 9a, it is evident that for k_{1d}>1, a segment of the root locus falls into the unstable region ($|\theta| < \frac{0.7\pi}{2}$), and this segment enlarges as k_{1d} increases. Fig. 9b illustrates that for $k_{1d}\leq$1, the entire root locus resides in the stable zone. Furthermore, reducing k_{1d} moves the locus further into the left half-plane, which positively influences stability.

Following the same procedure, the root locus is plotted for ω_c=10, α=0.7, k_{1d}=1, and a range of k_{2d} values, as shown in Fig. 10. The results indicate that for k_{2d}<1, part of the root locus extends into the unstable region. However, when $k_{2d}\geq$1, the root locus lies completely within the stable zone.

5.2. Dependence of Stability on the Bandwidth Parameter ω_c

To investigate the influence of the controller bandwidth, the root locus is generated for fixed parameters α=0.9, k_{1d}=1, k_{2d}=1.1, and varying ω_c, as presented in Fig. 11. The figure reveals that as ω_c increases, the root locus moves leftward, distancing itself from the instability boundary and thus enhancing stability. Nevertheless, a larger ω_c also leads to increased high-frequency noise and overshoot. Consequently, careful tuning of ω_c is required to balance these competing effects.

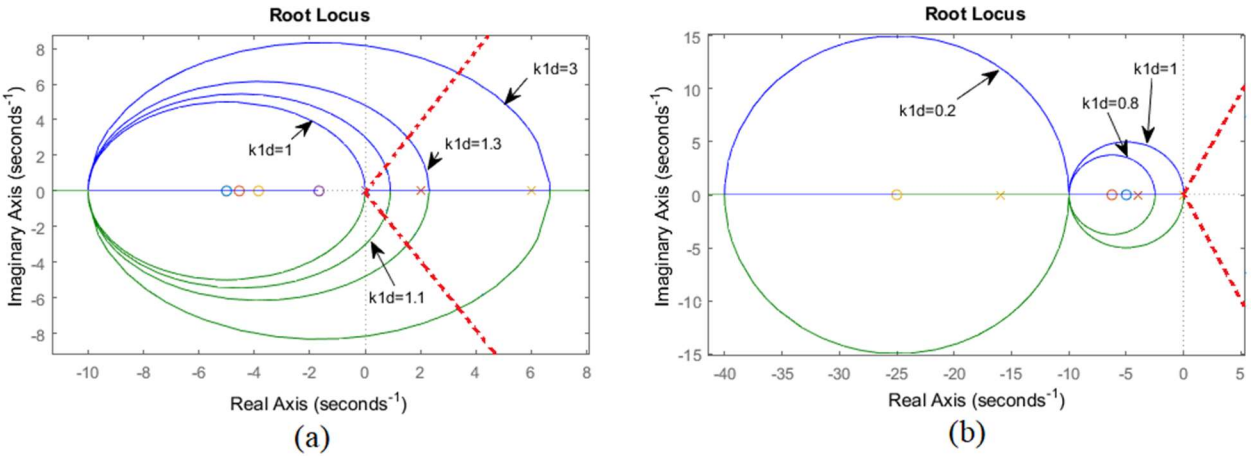

Fig. 9: Root locus corresponding to the DFIG rotor equivalent circuit with FFADRC under varying k_{1d} (with α=0.7, k_{2d}=1, ω_c=10): (a) $k_{1d}\geq 1$; (b) $k_{1d}\leq 1$.

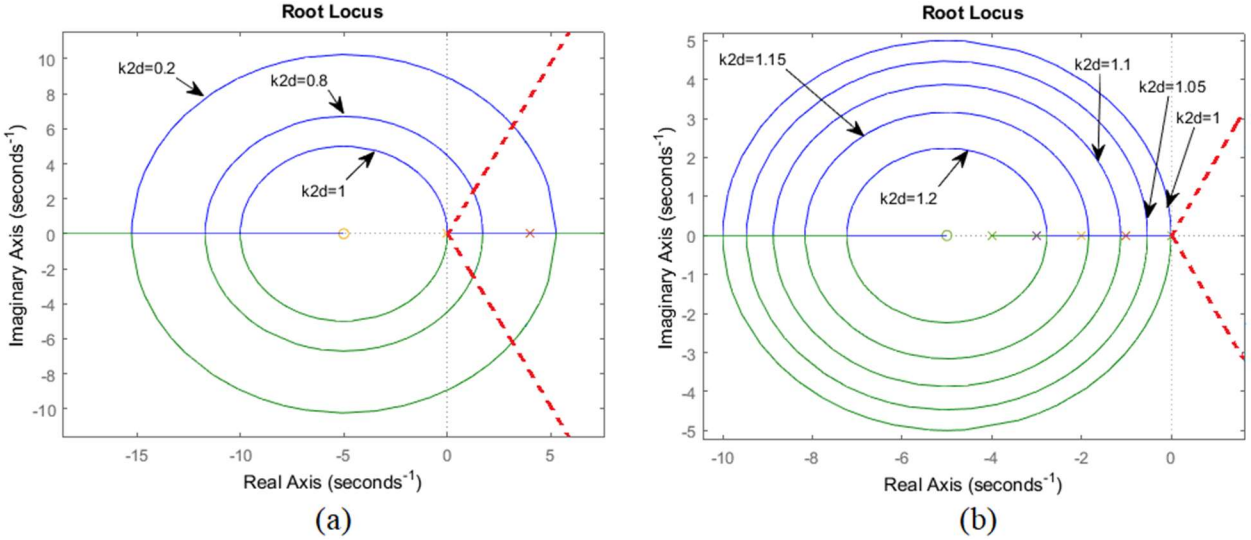

Fig. 10: Root locus corresponding to the DFIG rotor equivalent circuit with FFADRC under varying k_{2d} (with α=0.7, k_{1d}=1, ω_c=10): (a) $k_{2d}\leq 1$; (b) $k_{2d}\geq 1$.

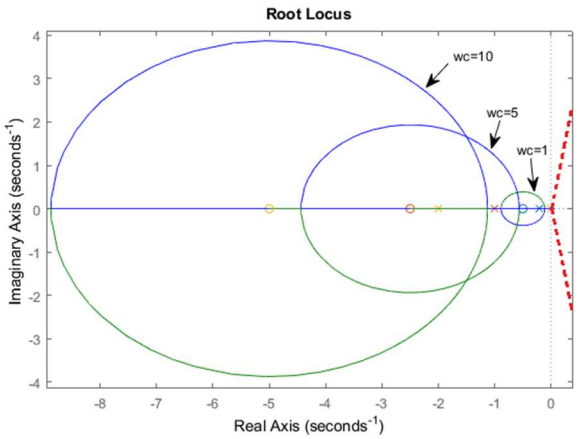

Fig. 11: Root locus of the DFIG rotor equivalent circuit with FFADRC for α=0.9, k_{1d}=1, k_{2d}=1.1, and different values of ω_c. (The red line indicates the stability boundary, defined by $|\theta| = \frac{0.9\pi}{2}$)

5.3. Influence of the Commensurate Order α on System Stability

Examining Eq. 46 reveals that if only α is varied while keeping other parameters constant, the poles and zero remain unchanged, and thus the root locus does not move. With $k_{2d}>k_{1d}$, the zero and one pole are in the left half-plane, and the remaining pole is at the origin, resulting in a stable system as long as $\alpha<1$. For $\alpha>1$, the unstable region encompasses not only the right half-plane but also parts of the second and third quadrants, which can lead to instability. This is illustrated in Fig. 12 for the case α=1.8, k_{1d}=1, k_{2d}=1.1, and ω_c=10. The figure clearly shows that a portion of the root locus enters the unstable region, an unacceptable condition.

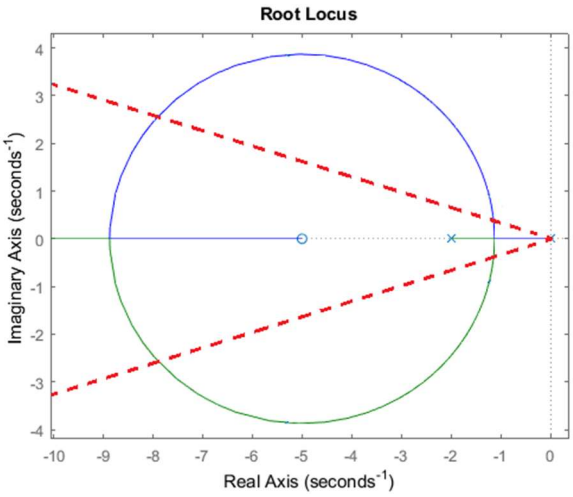

Fig. 12: Root locus analysis of the DFIG rotor equivalent circuit using FFADRC for α=1.8, k_{1d}=1, k_{2d}=1.1, and ω_c=10. The red line marks the stability boundary at $|\theta| = \frac{1.8\pi}{2}$, showing portions of the locus in the unstable region.

6. GSC Control Strategy

The control scheme for the GSC is presented in Fig. 13. The reference value of the active power exchanged with the grid (P_g^{ref}) is generated from the error between the actual DC-link voltage (V_{bus}) and its reference (V_{bus}^{ref}). The active and reactive power exchanged with the grid are given by the following equations [43]:

$$\begin{cases} P_g = \frac{3}{2}\left(v_{dg} i_{dg} + v_{qg} i_{qg}\right) \\ Q_g = \frac{3}{2}\left(v_{qg} i_{dg} - v_{dg} i_{qg}\right) \end{cases} \quad (50)$$

where i_{dg} and i_{qg} are the d-q components of the GSC output current, and v_{dg} and v_{qg} are the d-q components of the grid voltage. Under the condition that the d-axis of the synchronous reference frame is oriented along the grid voltage space vector, we have v_{qg}=0 and v_{dg}=$|v_g|$ (with $|v_g|$ being the magnitude of the grid voltage space vector). From Eq. 50, it follows that:

$$\begin{cases} P_g = \frac{3}{2} v_{dg} i_{dg} \quad \Rightarrow \quad i_{dg} = \frac{2}{3 v_{dg}} P_g \\ Q_g = \frac{-3}{2} v_{dg} i_{qg} \Rightarrow \quad i_{qg} = \frac{-2}{3 v_{dg}} Q_g \end{cases} \quad (51)$$

As illustrated in Fig. 13, the three-phase GSC output currents i_{ag}, i_{bg}, and i_{cg} are transformed to the stationary $\alpha\beta$ reference frame and then to the synchronous dq reference frame before being fed into the PI controllers. The angle θ_g of the grid voltage, necessary for these coordinate transformations, is determined using a phase-locked loop (PLL). The GSC output voltages (with respect to the load neutral point) expressed in the dq reference frame are as follows [43]:

$$\begin{cases} v_{df} = R_f i_{dg} + L_f \frac{di_{dg}}{dt} + v_{dg} - \omega_s L_f i_{qg} \\ v_{qf} = R_f i_{qg} + L_f \frac{di_{qg}}{dt} + v_{qg} + \omega_s L_f i_{dg} \end{cases} \quad (52)$$

The reference voltages v_{df} and v_{qf} are produced by two PI regulators according to Eq. 52. These quantities are then transformed through successive coordinate conversions to obtain the three-phase voltages corresponding to the GSC output. The resulting voltages are fed into the PWM modulator to generate the switching signals $S_{a\text{-}g}$, $S_{b\text{-}g}$, and $S_{c\text{-}g}$.

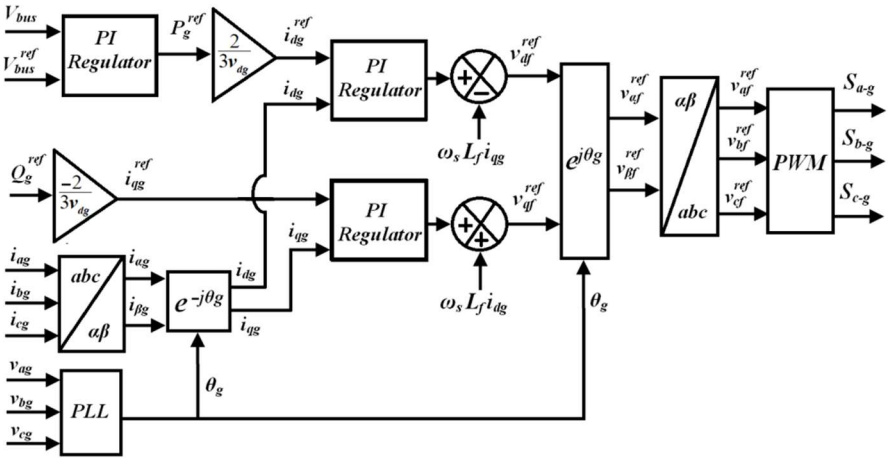

Fig. 13: Control block diagram of the GSC using vector orientation [43].

7. Simulation Results and Discussion

In this section, the WECS incorporating a DFIG is simulated. The DFIG is equipped with a back-to-back converter, and the FFADRC method is employed to control the RSC. The simulation parameters are summarized in Table 3. To evaluate the tracking performance of the FFADRC, the reference speed is alternately set to ω_s and $0.9\omega_s$. Based on the values in Table 3, $\omega_s=50\pi=157$ rad/s (mechanical). Simultaneously, the rotor speed is estimated using the speed estimator described by Eq. 35. The resulting machine speed waveforms are presented in Figs. 14 and 15.

At t=3.2 s, the reference speed changes from $0.9\omega_s$ to ω_s, and at t=4.2 s, it returns to $0.9\omega_s$. After approximately 2.5 s, the system reaches steady state, and the actual DFIG speed closely tracks the reference speed, confirming the effective performance of the FFADRC. Moreover, the estimated speed follows the actual speed with only a minor deviation, thereby validating the accuracy of the proposed speed estimation method.

Table 3: System parameters for the DFIG-based WECS simulation

Parameter	Value
Stator frequency (Hz)	50
Nominal power of stator (Mw)	2
Nominal rotational speed (rpm)	1500
Nominal voltage of stator (v)	690
Nominal current of stator (A)	1760
Nominal electromagnetic torque (N.m)	12732
pole pairs	2
Stator turns to the rotor turns	1/3
Nominal voltage of rotor (v)	2070
Stator resistance (mΩ)	2.6
Leakage inductance of stator and rotor (mH)	0.087
Magnetizing inductance (mH)	2.5
Rotor resistance referred to the stator (mΩ)	2.9
DC bus voltage referred to the stator (v)	1150
Moment of inertia (Kg.m^2)	127
Damping coefficient	0.001
Switching frequency of PWM (kHz)	2
Sampling time (μs)	50
Gearbox ratio	100
Radius of turbine blades (m)	42
Air density (kg/m^3)	1.225
DC bus capacitance (mF)	80
Grid side filter's resistance (μΩ)	20
Grid side filter's inductance (μH)	400
The r parameter corresponds to the FTD block (d & q axes)	5*10^6
Approximation order of fractional blocks	1
The bandwidth of FESO (d & q axes)	250
The bandwidth of FFOADRC (d & q axes)	50
The fractional order of FTD and FESO (d & q axes)	0.9
The parameters of FFOADRC (k_{1d} & k_{1a})	0.9
The parameters of FFOADRC (k_{2d} & k_{2a})	1.1

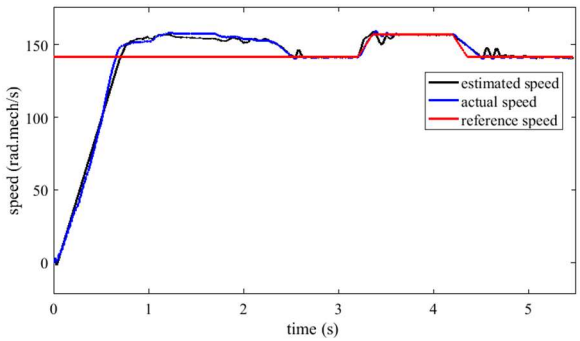

Fig. 14: DFIG speed response with FFADRC (red: reference speed, black: estimated speed, blue: actual speed).

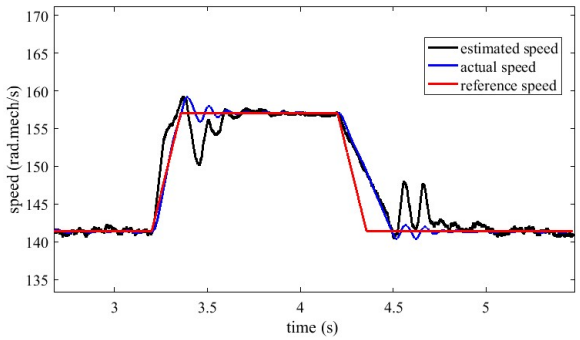

Fig. 15: Zoomed region of Fig. 14 highlighting the speed tracking accuracy.

The steady-state d- and q-axis rotor current waveforms are shown in Figs. 16 and 17, respectively. It can be observed that the actual currents closely track their reference values, demonstrating the effectiveness of the proposed sensorless vector control strategy. Similarly, the d- and q-axis output currents of the GSC are presented in Figs. 18 and 19. The accurate tracking of the reference currents by the actual GSC currents further validates the proper operation of the vector control scheme for the GSC.

8. Evaluation of FFADRC Robustness Against Internal and External Disturbances

This section separately analyzes the impact of two types of disturbances: external disturbances caused by wind speed changes and internal disturbances resulting from DFIG parameter variations.

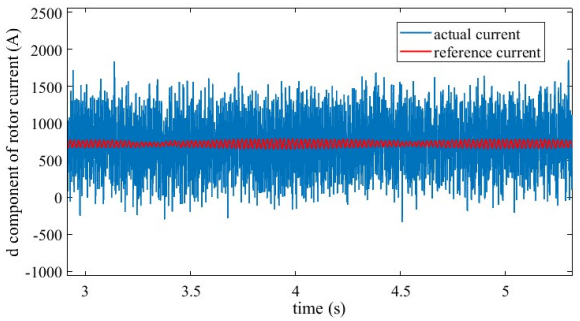

Fig. 16: d-axis rotor current at steady state (blue: actual, red: reference).

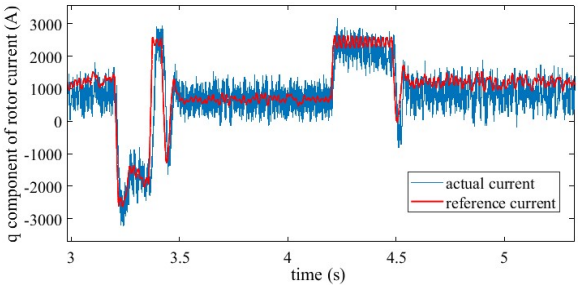

Fig. 17: *q*-axis rotor current at steady state (blue: actual, red: reference).

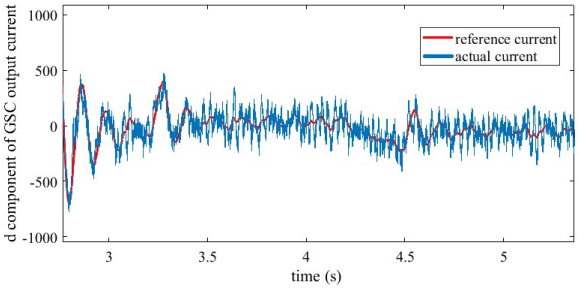

Fig. 18: *d*-axis component of the GSC output current (blue: actual value, red: reference value).

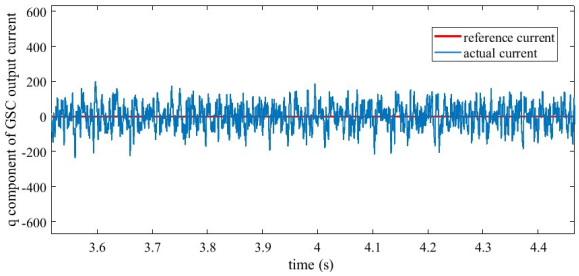

Fig. 19: *q*-axis component of the GSC output current (blue: actual value, red: reference value).

8.1. Impact of External Disturbances on the FFADRC-Controlled DFIG

The robustness of the controller against external disturbances is assessed by applying wind speed variations according to the profile in Fig. 20, while maintaining the reference speed constant at ω_s. The corresponding speed waveforms are presented in Figs. 21–23. It can be observed that, despite successive wind speed changes at 2.75, 3.75, and 4.75 seconds, the actual speed rapidly tracks the reference speed, indicating the successful attenuation of external disturbances by the FFADRC.

Fig. 24 illustrates the DFIG electromagnetic torque response under varying wind speed conditions. As the wind speed increases at 2.75 s, the actual and reference torque values rise accordingly. Conversely, at 3.75 s and 4.75 s, the torque decreases in response to the reduction in wind speed, indicating proper DFIG operation. The accurate tracking of the reference torque by the actual torque further validates the disturbance rejection capability of the FFADRC.

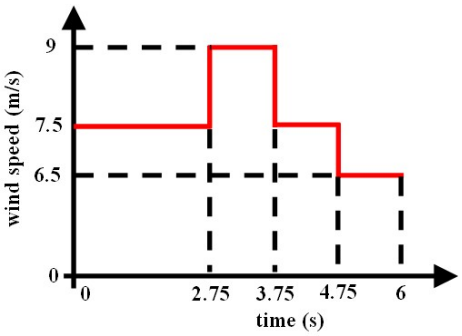

Fig. 20: Wind speed variation profile used for external disturbance evaluation.

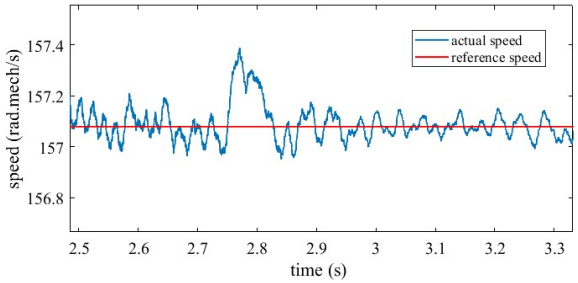

Fig. 21: Speed tracking performance of the FFADRC-controlled DFIG following a wind speed disturbance at t=2.75 s (red: reference speed, blue: actual speed).

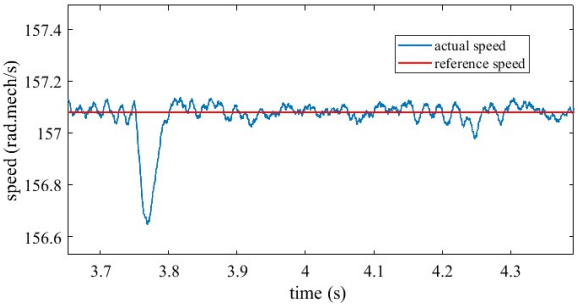

Fig. 22: Speed tracking performance of the FFADRC-controlled DFIG following a wind speed disturbance at t=3.75 s (red: reference speed, blue: actual speed).

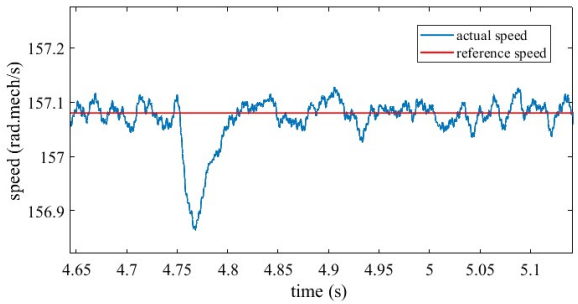

Fig. 23: Speed tracking performance of the FFADRC-controlled DFIG following a wind speed disturbance at t=4.75 s (red: reference speed, blue: actual speed).

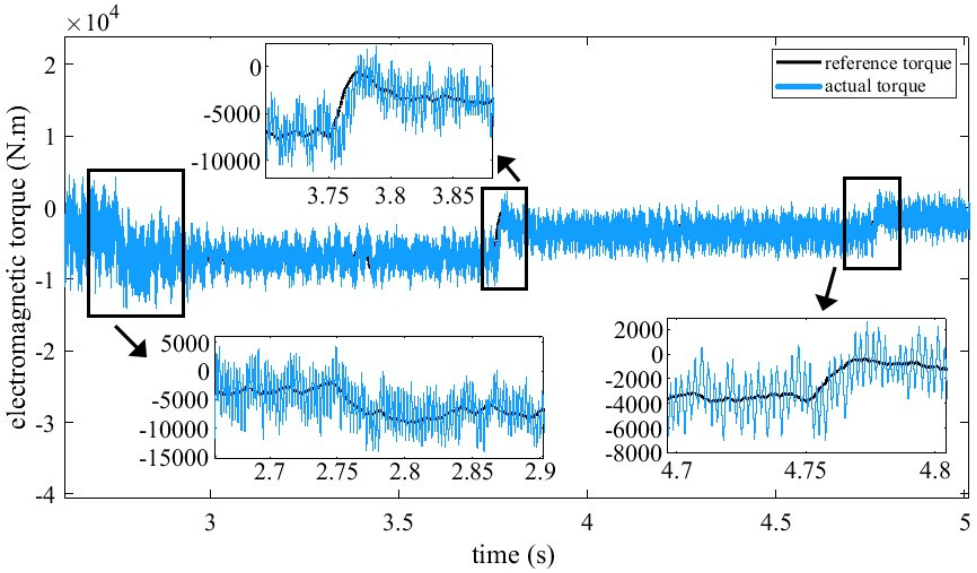

Fig. 24: Electromagnetic torque tracking performance of the FFADRC-controlled DFIG under external disturbances (reference torque in black, actual torque in blue)

8.2. Impact of Internal Disturbances on the FFADRC-Controlled DFIG

The impact of internal disturbances is investigated by introducing changes in the DFIG parameters, namely the rotor resistance and rotor inductance. As listed in Table 3, the nominal values are R_r=2.9 mΩ and L_r=2.5+0.087=2.587 mH.

To further evaluate the robustness of the controller against internal disturbances, the rotor resistance and rotor inductance are individually subjected to step variations of 10% and 20%. The exact parameter values and the timing of each change are detailed in Tables 4 and 5. During these tests, the reference speed is held constant at $0.9\omega_s$. Figs. 25 and 26 illustrate the speed waveforms corresponding to the variations in rotor resistance and rotor inductance, respectively. As illustrated in these figures, step changes in rotor resistance and inductance induce oscillations in the actual speed around the reference. The rapid damping of these oscillations confirms the robustness of the FFADRC in rejecting internal disturbances and preserving speed tracking accuracy.

Table 4: Rotor resistance variation profile

Time range (s)	Rotor resistance value
t<3.65	R_r
3.65<t<4.1	1.1* R_r
4.1<t<4.5	0.9* R_r
4.5<t<5	1.2* R_r
5<t<6	0.8* R_r

Table 5: Rotor inductance variation profile

Time range (s)	Rotor inductance value
t<3.55	L_r
3.55<t<4.5	1.1* L_r
4.5<t<5	0.9* L_r
5<t<5.5	1.2* L_r
5.5<t<6	0.8* L_r

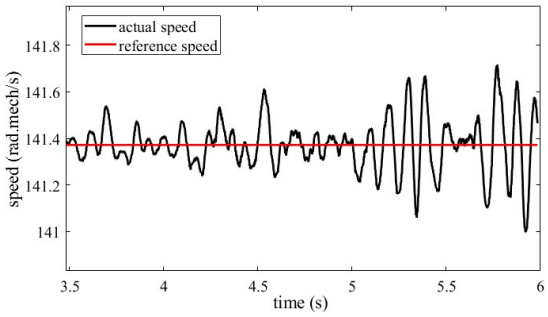

Fig. 25: DFIG speed response with FFADRC under rotor resistance variations applied at t=3.65, 4.1, 4.5, and 5.0 seconds (red: reference speed, black: actual speed).

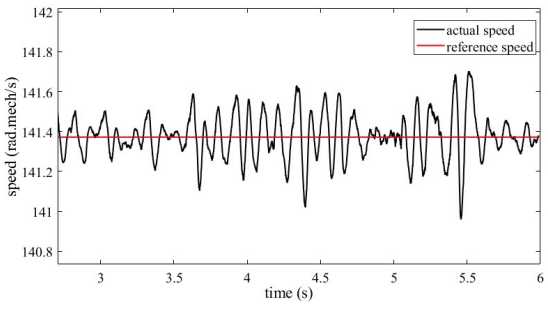

Fig. 26: DFIG speed response with FFADRC under rotor inductance variations applied at t=3.55, 4.5, 5.0, and 5.5 seconds (red: reference speed, black: actual speed).

9. Comparative Study of ADRC, Fuzzy ADRC, Fractional-Order ADRC, and FFADRC

Consider a second-order SISO nonlinear fractional-order system, as introduced in Eq. 19. For the purpose of comparison, the following transfer function is adopted as a test system:

$$\frac{\mathbf{Y(s)}}{\mathbf{U(s)}} = \frac{\mathbf{10}}{\mathbf{s^{1.8}} + 3\boldsymbol{s}^{0.9} + 2} \tag{53}$$

where *U(s)* and *Y(s)* represent the system input and output, respectively. The system's commensurate order is α=0.9. A comparative evaluation of ADRC, fuzzy ADRC, fractional-order ADRC, and FFADRC is conducted by applying a unit step input to the system. At t=0.5 s, step disturbances of amplitudes 50 and 5000 are injected separately to assess the controllers' responses to weak and severe disturbances, respectively. The corresponding results are illustrated in Figs. 27 and 28. The results demonstrate that fractional-order ADRC and FFADRC provide faster transient responses and more effective disturbance rejection compared to ADRC and fuzzy ADRC. Following the disturbance at 0.5 s, both controllers rapidly restore the output to its reference without noticeable oscillations. Furthermore, FFADRC outperforms fractional-order ADRC in terms of convergence speed after the disturbance. In contrast, ADRC and fuzzy ADRC exhibit poor disturbance rejection capabilities for both weak and severe disturbances, as evident from Figs. 27 and 28.

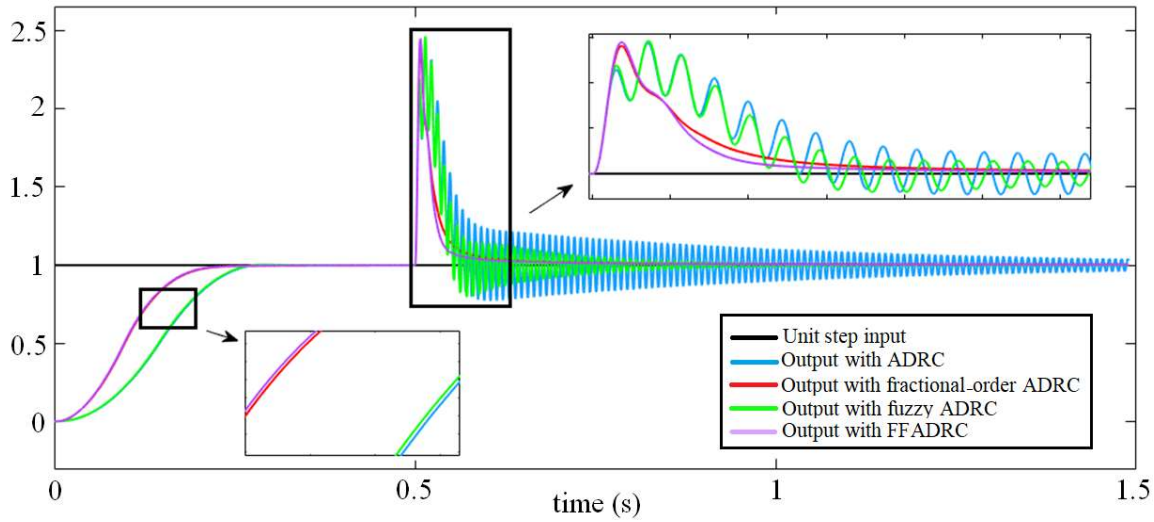

Fig. 27: Comparison of system output with various ADRC strategies under a severe step disturbance of 5000 applied at t=0.5 s (black: unit step input, blue: ADRC, purple: FFADRC, green: fuzzy ADRC, red: fractional-order ADRC)

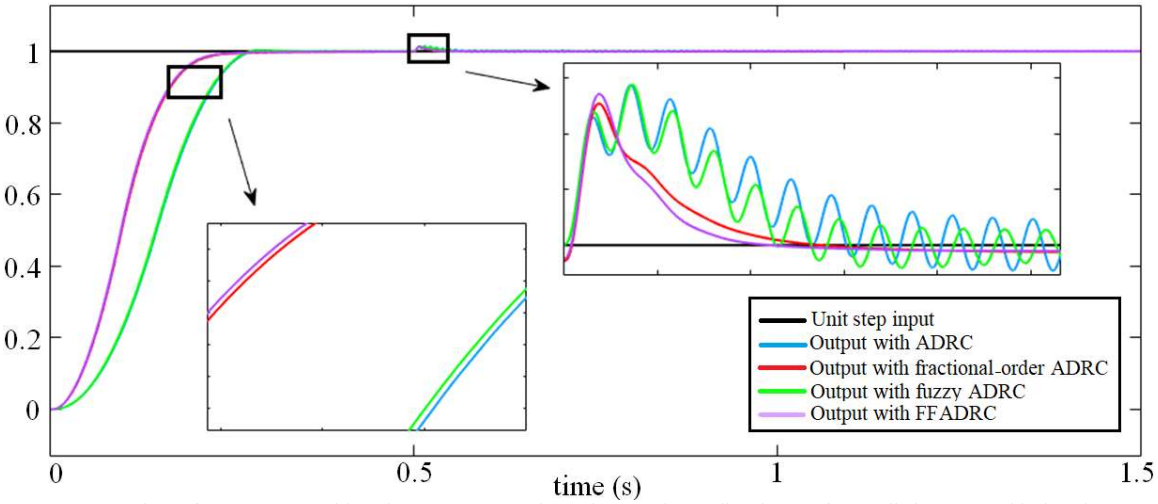

Fig. 28: Comparison of system output with various ADRC strategies under a weak step disturbance of 50 applied at t=0.5 s (black: unit step input, blue: ADRC, purple: FFADRC, green: fuzzy ADRC, red: fractional-order ADRC)

10. Conclusion and Future Work

This paper has presented a novel sensorless vector control strategy for DFIG-based wind turbines using a FFADRC. The proposed approach effectively eliminates the need for mechanical encoders by estimating the rotor speed directly from the control laws and the disturbances estimated by a FESO. By integrating fuzzy logic for online tuning of the LSEF coefficients and employing fractional-order operators in both TD and ESO, the controller achieves enhanced flexibility, improved disturbance rejection, and robust performance under various operating conditions.

Extensive simulation studies have validated the effectiveness of the FFADRC method. The results demonstrate accurate speed tracking, rapid convergence, and strong resilience against external disturbances such as wind speed variations, as well as internal disturbances caused by DFIG parameter changes (e.g., rotor resistance and inductance variations). Comparative analysis with conventional ADRC, fuzzy ADRC, and fractional-order ADRC confirms that the proposed FFADRC offers superior transient response, faster disturbance rejection, and better overall dynamic performance. Stability analysis using the root locus technique further verified the robustness of the controller across a wide range of design parameters.

Future work will focus on the experimental validation of the FFADRC strategy on a laboratory-scale DFIG test bench to assess its real-time performance and practical feasibility. Moreover, extending the proposed method to the coordinated control of entire wind farms, considering wake effects and grid integration challenges, is a promising direction. The integration of machine learning techniques for adaptive parameter tuning and the incorporation of predictive control elements to further enhance the response under severe grid faults are also suggested for further investigation. Finally, the application of the FFADRC concept to other power electronic converters and renewable energy systems could be explored to generalize its benefits.

References

[1] Nunes M V A, Lopes J A P, Zurn H H, Bezerra U H, Almeida R G. Influence of the variable-speed wind generators in transient stability margin of the conventional generators integrated in electrical grids. *IEEE Trans Energy Conver*. 2004, 19(4): 692–701.

[2] Blaabjerg F, Liserre M, Ma K. Power Electronics Converters for Wind turbine Systems. *IEEE Trans Indust Appl*. 2012, 48(2).

[3] Bouderbala M, Bossoufi B, Lagrioui A, Taoussi M, Aroussi H A Ihedrane Y. Direct and indirect vector control of a doubly fed induction generator based in a wind energy conversion system. *Int J Elect Comput Eng* (IJECE). 2018, 9(3):1531–1540, doi: 10.11591/ijece.v9i3.pp1531-1540.

[4] Chen S Z, Cheung N C, Wong K C Wu J. Integral variable structure direct torque control of doubly fed induction generator. *IET Renew Power Gener*. 2011, 5(1): 18–25, doi: 10.1049/iet-rpg.2009.0021.

[5] Benbouhenni H. Comparative Study between Different Vector Control Methods Applied to DFIG Wind Turbines. *Majlesi J Mechatro Syst*. 2018, 6 (4): 15-23, Online-issn: 2322-1089.

[6] Guo B Z, Zhao Z L. Active Disturbance Rejection Control for Nonlinear Systems: An Introduction. New York: John Wiley & Sons; 2016, Online isbn: 9781119239932, doi: 10.1002/9781119239932.

[7] Essadki A, Annoukoubi M, Nasser T. A Novel Adaptive Active Disturbance Rejection Control Strategy to Improve the Stability and Robustness for a Wind Turbine Using a Doubly Fed Induction Generator. *J Electr Comput Eng*. 2020, hindawi, doi: 10.1155/2020/9847628.

[8] Chowdhury M A, Sayem A H M, Shen W, Islam K S. Robust active disturbance rejection controller design to improve low-voltage ride-through capability of doubly fed induction generator wind farms. *IET Renew Power Gener*. 2015, 9(8): 961–969.

[9] Boukhriss A, Essadki A, Bouallouch A, Nasser T. Maximization of Generated Power from Wind Energy Conversion Systems using a Doubly Fed Induction Generator with Active Disturbance Rejection Control. Paper presented at: 2014 Second World Conference on Complex Systems (WCCS); IEEE Conference, 2014, 330-335.

[10] Ebrahim O S, Jain P K. Robust State Control with Narrowband Disturbance Rejection for Wind Driven DFIG under Grid Voltage Unbalance. Paper presented at: 2009 IEEE Electrical Power & Energy Conference; 2009.

[11] De Z, Shengwei M, Feng L, Jian S. Power Oscillation Damping Controller Based on Active Disturbance Rejection Control Technique for DFIG-Based Wind Turbine Generators. Paper presented at: 2014 The 26th Chinese Control and Decision Conference (2014 CCDC); IEEE Conferences, 2014, 2749-2752.

[12] Guo L, Wang D, Diao L, Peng Z. Active Disturbance Rejection Control for an Unbalanced Stand-alone Doubly Fed Induction Generator. Paper presented at: 2016 The 35th Chinese Control Conference (CCC); IEEE Conferences, 2016, 8721-8726.

[13] Guo L, Wang D, Peng Z, Diao L. Active Disturbance Rejection Control for Stand-Alone Doubly Fed Induction Generator. Paper presented at: 2016 The 28th Chinese Control and Decision Conference (CCDC); 2016, 6164-6168.

[14] Patel D, Zhao L. Active Disturbance Rejection Control of Doubly-Fed Induction Generator during Voltage Dip. Paper presented at: 2010 ESA Annual Meeting on Electrostatics Proceedings; paper D4, 2010.

[15] Ali M, Alexander C K. Trajectory Tracking Control for a Robotic Manipulator Using Nonlinear Active Disturbance Rejection Control. Paper presented at: 2017 The ASME Dynamic Systems and Control Conference Proceedings (DSCC2017); Tysons, Virginia, USA, 2017.

[16] Luo H, Cheng H, Wang J. A Cascade Linear Active Disturbance Rejection Controller for Vector Control

System of PMSM. Paper presented at: 2015 The 3rd International Conference on Mechatronics, Robotics and Automation (ICMRA 2015); 2015, 1076-1082.
[17] Kimathi S M. Design of an Online Adaptive Controller For Active Disturbance Rejection In a Fixed Wing UAV Using Reinforcement Learning And Differential Games. *Jomo Kenyatta University of Agriculture and Technology*, 2018.
[18] Pena R, Cardenas R, Proboste J, Asher G, Clare J. Sensorless Control of Doubly-Fed Induction Generators Using a Rotor-Current-Based MRAS Observer. *IEEE Trans Indust Electr.* 2008, 55 (1).
[19] Messaoudi M, Kraiem H, Hamed M B, Sbita L, Abdelkrim M N. A Robust Sensorless Direct Torque Control of Induction Motor Based on MRAS and Extended Kalman Filter. *Leonar J Sci*. 2008, 35-56, issn 1583-0233.
[20] Ta C M, Uchida T, Hori Y. MRAS-based Speed Sensorless Control for Induction Motor Drives Using Instantaneous Reactive Power. Paper presented at: 2001 The 27th Annual Conference of the IEEE Industrial Electronics Society; IEEE, 2001, 1417-1422.
[21] Ghossini H A. Contributions to the study of control for small-scale wind turbine connected to electrical microgrid with and without sensor. *Thèse présentée pour l'obtention du grade de Docteur de l'UTC*. Universite de Technologie Compiegne, 2016.
[22] Szabat K, Serkies P J. Design and Analysis of the Luenberger Observers for Three-Inertia System. 2009, 329-340.
[23] Zhang Y, Zhao Z, Lu T, Yuan L, Xu W, Zhu J. A Comparative Study of Luenberger Observer, Sliding Mode Observer and Extended Kalman Filter for Sensorless Vector Control of Induction Motor Drives. 2009 IEEE Energy Conver Cong Expos. 2009, 2466-2473, doi: 10.1109/ECCE.2009.5316508.
[24] Smidl V, Peroutka Z. Advantages of Square-Root Extended Kalman Filter for Sensorless Control of AC Drives. *IEEE Trans Indust Electr*. 2011, doi: 10.1109/TIE.2011.2180273.
[25] Pan C T, Juan Y L. A novel sensorless MPPT controller for a high-efficiency micro-scale wind power generation system. *IEEE Trans Energy Conver*. 2010, 25: 207–216.
[26] Xu L, Cartwright P. Direct active and reactive power control of DFIG for wind energy generation. *IEEE Trans Energy Conver*. 2006, 21(3): 750-758.
[27] Cardenas R, Pena R. Sensorless vector control of induction machines for variable-speed wind energy applications. *IEEE Trans Energy Conver*. 2004, 19(1): 196–205.
[28] Chakib R, Essadki A, Cherkaoui M. Active Disturbance Rejection Control for Wind System Based on a DFIG. *Int J Electr Comput Eng*. World Academy of Science, Engineering and Technology, 2014, 8(8).
[29] Benelghali S, El Hachemi Benbouzid M, Charpentier J, Ahmed-Ali T, Munteanu I. Experimental validation of a marine current turbine simulator: Application to a permanent magnet synchronous generator based system second-order sliding mode control. *IEEE Trans Indust Electr*. 2011, 58(1): 118–126.
[30] Slootweg J, De Haan S, Polinder H, Kling W. General model for representing variable speed wind turbines in power system dynamics simulations. *IEEE Trans Power Syst*. 2003, 18(1): 144–151.
[31] Evangelista C, Valenciaga F, Puleston P. Active and reactive power control for wind turbine based on a mimo 2-sliding mode algorithm with variable gains. *IEEE Trans Energy Conver*. 2013, 28(3): 682–689.
[32] Abu-Rub H, Malinowski M, Al-Haddad K. Power Electronics for Renewable Energy Systems, Transportation and Industrial Applications. New York: John Wiley & Sons; 2014, doi: 10.1002/9781118755525.
[33] Girsang I, Dhupia J, Muljadi E, Singh M, Pao L. Gearbox and drive train models to study dynamic effects of modern wind turbines. *IEEE Trans Indust Appl*. 2014, 50(6): 3777–3786.
[34] Houcine B, Bousserhane I K, Bousmaha B, Abdelkader H, Tahar B. Vector Control of Wind Turbine Conversion chain Variable Speed Based on DFIG Using MPPT Strategy. *International Journal of Applied Engineering Research.* 2018, 13(7): 5404-5410, issn 0973-4562.
[35] Melicio R, Mendes V M F, Catalao J P S. Comparative study of power converter topologies and control strategies for the harmonic performance of variable-speed wind turbine generator systems. *Energy Elsevier*, 2011, 36(1): 520-529, doi: 10.1016/j.energy.2010.10.012.
[36] Boukhriss A, Nasser T, Essadki A. A Linear Active Disturbance Rejection Control applied for DFIG based Wind Energy Conversion System. *Int J Comput Sci Issues (IJCSI)*. 2013, 10(2): 391-399.
[37] Han J. From PID to auto disturbances rejection control. *IEEE Trans Indust Electr*. 2009, 56(3): 900-906.
[38] Herbst G. A Simulative Study on Active Disturbance Rejection Control (ADRC) as a Control Tool for Practitioners. 2013, 246-279, doi: 10.3390/electronics2030246.
[39] Song J, Gao K, Wang L, Yang E. Comparison of linear and nonlinear active disturbance rejection control method for hypersonic vehicle. Paper presented at: 2016 The 35th Chinese Control Conference (CCC); IEEE, 2016, doi: 10.1109/ChiCC.2016.7555064.
[40] Peng N, Bai Y, Luo H, Bai J. Artillery Position Control through Auto Disturbance Rejection Controller Based-on Fuzzy Control. Paper presented at: 2013 The 5th International Conference on Intelligent Human-Machine Systems and Cybernetics; 2013, doi: 10.1109/IHMSC.2013.124.
[41] Petráš I. Stability of fractional-order systems with rational orders. *Math dynam syst.* 2008, 1-25, arXiv:0811.4102v2.
[42] Gao Z. Active disturbance rejection control for nonlinear fractional-order systems. *Int J robust nonlinear cont*. New York: John Wiley & Sons; 2015, 26: 876-892, doi: 10.1002/rnc.3344.
[43] Abad G, López J, Rodríguez M A, Marroyo L, Iwanski G. Doubly Fed Induction Machine: Modeling and Control for Wind Energy Generation. New York: John Wiley & Sons; 2011, isbn: 978-1-118-10494-1.